Phase-Resolved Electron Guiding in Optimized Chip-Based Microwave Potentials

Jakob Hammer,[1,2,*] Johannes Hoffrogge,[2] Stephan Heinrich,[1,2] and Peter Hommelhoff[1,2]

[1]*Department für Physik, Friedrich-Alexander-Universität Erlangen-Nürnberg, Staudtstrasse 1, 91058 Erlangen, Germany*

[2]*Max Planck Institute of Quantum Optics, Hans-Kopfermann-Strasse 1, 85748 Garching, Germany*

(Received 18 June 2014; revised manuscript received 2 October 2014; published 27 October 2014)

Surface-electrode chips are a versatile and well-established tool for trapping and guiding charged particles. The technique, usually applied to ions, has recently been adapted for electrons using a two-dimensional quadrupole guide at microwave driving frequencies. During injection into the guiding potential, the electron trajectories show a strong dependence on the phase and amplitude of fringing electric fields at the coupling entrance of the guide. Here we study the corresponding electron dynamics using a pulsed electron source with pulse durations of several 100 ps to temporally resolve fringing electric fields oscillating at the microwave drive frequency. By synchronizing the timing of the electron pulses to a certain microwave phase, we can increase the electron guiding efficiency by 50%. Furthermore, we present numerically optimized electrode structures for which the amplitude of fringing electric fields at the coupling entrance of the guide is drastically reduced. Particle-tracing simulations suggest that the optimized electrode layout allows the direct injection of electrons into the lowest-lying motional quantum states of the transverse guiding potential.

DOI: 10.1103/PhysRevApplied.2.044015

I. INTRODUCTION

Coherent electron beams have enabled the demonstration of matter-wave diffraction [1] and interference [2,3] and have provided fundamental insight into quantum effects like the Hanbury Brown–Twiss anticorrelations of free electrons [4] and decoherence effects near conducting surfaces [5]. The profound analogy to phenomena typically known from light optics also involved the development of electron-optical devices like coherent beam splitters and sophisticated imaging optics. Accordingly, all these experiments relied on conventional electron optics using electrostatic and magnetic fields to shape the transverse properties of the electron beam. Here we focus on the quantum-mechanical control of the transverse motion of an electron wave packet by means of microwave electric fields above the surface of a planar chip. The transverse confinement of a coherent electron beam using this technique will augment the already available electron toolkit by a wholly new set. For example, planar microwave chips are well suited for the implementation of electron resonators and beam splitters.

Quantum control over the motional degrees of freedom of atomic matter waves on a planar chip forms a common basis for various research areas such as quantum-information processing with trapped ions [6–9] or guided matter-wave optics with neutral atoms [10,11]. Surface-electrode ion traps [6,12] have been shown to provide finely structured potential landscapes such as junctions for trapped ions [13] or double-well potentials where the small distances between the potential minima allow the direct coupling of separately trapped ions via the Coulomb force [14,15]. Furthermore, this technology allows the interfacing of trapped ions to other systems integrated in the chip layout like optical components [16–19], microwave transmission lines [20,21], or superconducting systems [22,23].

Here we discuss the manipulation of electrons on a planar microwave chip that allows for tight transverse confinement of electrons by purely electric fields [24,25]. The guiding of electrons on a planar microwave chip is based on a linear quadrupole guide, similar to existing surface-electrode ion traps. As a result of the much higher charge-to-mass ratio of electrons, we need to operate the planar microwave structures with driving frequencies in the gigahertz range. As a consequence, stable confinement of slow electrons with energies below 10 eV can be achieved with trapping frequencies ranging from 100 to 1000 MHz. Quantum-mechanical control of the transverse motion of electrons in such a guide will enable new quantum-optics experiments with electrons such as guided matter-wave interferometry or noninvasive electron microscopy [26]. Here the transverse motional quantum state of the electron can be used as a carrier of quantum information. Additionally, low-energy guided or trapped electrons may be used for the controlled collisional excitation of Rydberg atoms [27] or could be coupled to superconducting structures for quantum-information processing [28].

A prerequisite for these experiments is the preparation of electrons in low-lying quantum states of the transverse guiding potential. The corresponding quantum-mechanical ground state has a spatial extension on the order of 100 nm,

*jakob.hammer@fau.de

which can be resolved by conventional electron optics. With a well-collimated, diffraction-limited electron gun, it should, thus, be possible to directly inject electrons into the transverse motional ground state. This can be achieved by matching the wave function of an incoming electron wave packet to the ground state of the guiding potential. In addition to a diffraction-limited electron gun, this method necessitates a guiding potential that minimizes the excitations of the electrons during injection into the guide. Because of fringing electric fields at the edges of the guiding substrate, the electron beam experiences an initial deflection before it becomes injected into the guiding potential of the microwave chip. This leads to an excited motion of the electrons within the guiding potential or even a loss of electrons from the guide. Here we demonstrate two possible strategies to provide an adiabatic injection of electrons from free space into the guiding potential, thereby increasing the guiding efficiency and paving the way towards quantum-mechanical control of the guided electrons.

This paper is organized as follows. Section II recapitulates the basics of electron guiding on a planar microwave chip, which will be important for the understanding of the following sections. Section III presents particle-tracing simulations in order to study the dynamics of electrons after injection into the guide. These simulations reproduce the measured guiding signal and allow us to address the origin of an excited electron motion or loss of electrons from the guide. The first strategy to provide an adiabatic injection of electrons is presented in Sec. IV, where a numerical optimization of the electrode design shows that unwanted fringing electric fields at the edges of the guiding substrate can be efficiently reduced. By these means, the electron beam experiences a smooth passage from free space into the guiding potential. The second strategy focuses on temporally synchronizing the injection of electron pulses to a specific phase of the driving electric field, which leads to a minimization of the initial deflection of the electrons. In Sec. V we experimentally demonstrate the synchronization of a pulsed electron source to the driving field of the microwave guide and present phase-resolved measurements of the electron injection efficiency. A combination of both strategies should allow us to adiabatically couple electrons from free space into the ground state of the transverse guiding potential, as briefly discussed in the outlook in Sec. VI.

II. MICROWAVE GUIDING OF ELECTRONS

A. Planar microwave guiding structures

The guiding of electrons in the electric field of a planar microwave chip combines existing technology from surface-electrode ion traps [6,12,29] with electron matter-wave optics [30]. In contrast to conventional electron optics, where the transverse focusing is performed using static electromagnetic fields, the transverse confinement of guided electrons is provided by an oscillating, purely electric potential.

An electron can be confined in an electric potential $\phi(\vec{r},t)=\phi_{\mathrm{RF}}\cos(\Omega t)$ with amplitude ϕ_{RF} and angular frequency Ω, if the electric-field gradient an electron encounters on its excursion from the potential minimum is small during one cycle of the microwave driving signal. The electron then effectively experiences a time-averaged harmonic pseudopotential [31] given by $\Psi=[Q^2/(4M\Omega^2)]|\nabla\phi_{\mathrm{RF}}(\vec{r})|^2$. Here, Q and M denote the electron charge and mass.

Similar to surface-electrode ion traps, we use an approximately quadrupolar electric potential generated by a planar electrode structure on the surface of the microwave chip. Suitable electrode layouts may be obtained by conformal mapping of a circular electrode geometry onto the tangential plane [32]. The electric potential of the resulting planar electrode layout deviates from an ideal quadrupole potential only in higher orders of the multipole expansion.

The dynamics of an electron within the guide can be decomposed in a slow secular motion in the pseudopotential, with a frequency ω, and a superimposed, fast micromotion that oscillates approximately at the frequency of the driving electric field Ω. The secular oscillation in the pseudopotential is characterized by a transverse trap frequency $\omega=q/\sqrt{8}\ \Omega$ and a pseudopotential depth $U=[uq/(8\eta)]V_0$. Here, V_0 is the microwave voltage amplitude applied to the signal electrodes of the guiding structure. The stability parameter $q=\eta 2QV_0/(M\Omega^2R_0^2)$ quantifies the validity of the pseudopotential approximation, where stable confinement of an electron requires $0<q<0.9$. The micromotion is an indication for small deviations from the pseudopotential approximation. Its oscillation amplitude relative to the secular oscillation amplitude is given by a factor of $q/4$ [31]. The constants η and u can be derived from the conformal mapping of the planar electrode design and lead to a reduction of the potential depth compared to a circular electrode design. Figure 1 shows a simulation of the pseudopotential Ψ formed above the five-wire electrode geometry employed in this paper. Electrons traveling along the y direction, perpendicular to the image plane, are confined transversally in the minimum of the two-dimensional pseudopotential Ψ, which forms at a distance $R_0=500\ \mu$m above the substrate.

For the investigations in this paper, we use a five-wire geometry, where the central ground wire has a width $c=350\ \mu$m, the two microwave signal electrodes $w=750\ \mu$m, and the outer ground electrodes cover the remaining area of the chip. For this geometry, one finds $\eta=0.31$ and $u=0.0079$. The gaps between the conducting electrodes are laser machined into the 10-μm-thick gold layer and have a width of 15 μm. In order to provide stable confinement of electrons, we drive the signal electrodes

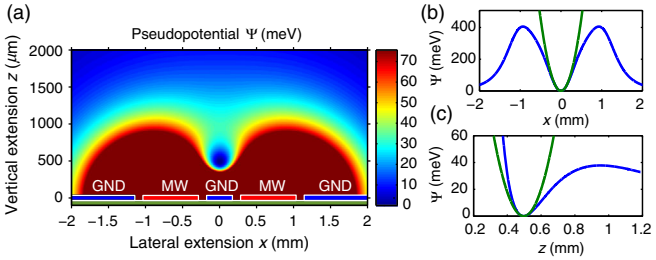

FIG. 1. Guiding potential in the pseudopotential approximation. (a) Pseudopotential Ψ in the x-z plane with a cross-sectional view of the electrodes. The height of the electrodes is exaggerated for better visibility. (b) Pseudopotential along the x direction (blue) with harmonic fit (green). (c) Pseudopotential along the z direction (blue) with harmonic fit (green). The confinement of electrons is weakest along the z direction with a potential depth of 30 meV.

with $V_0 = 29$ V at a frequency of $\Omega = 2\pi \times 996$ MHz, yielding a stability parameter of $q = 0.32$. From the horizontal and vertical cut through the potential minimum along the x and z axes shown in Figs. 1(b) and 1(c), we infer a trapping frequency $\omega = 2\pi \times 114$ MHz and a minimum potential depth $U = 30$ meV along the vertical dimension.

B. Guiding of electrons along a curve

Figure 2(a) shows a close-up of the experimental setup used for the electron guiding measurements. The electron gun is based on the widely used Erdman-Zipf design [33], which provides an electron beam with kinetic energies ranging from 1 to 10 eV, as needed for electron guiding.

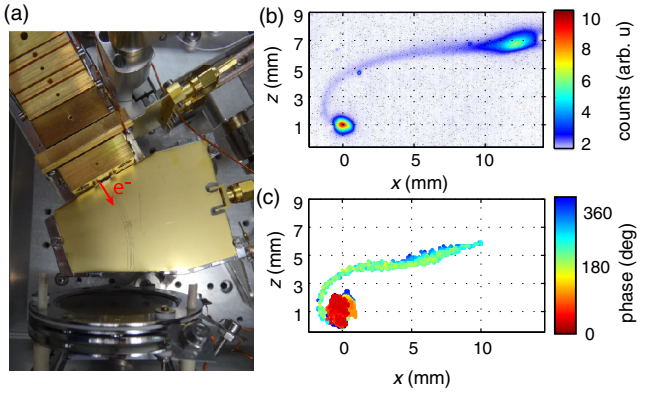

FIG. 2. Electron guiding experiment. (a) Photograph of the electron source (top left), microwave guiding chip (center), and the imaging electron microchannel-plate detector (bottom). Here the mu-metal shield and a gold-plated copper housing enclosing the experiment are removed. (b) Electron guiding signal with the guided electrons recorded at a position $x = 0$ mm. When the microwave drive is turned off, the unguided electron spot is detected at $x = 21$ mm (not shown). The color scale depicts the electron count rate. (c) Simulated guiding signal. Here the color scale corresponds to the phase of the microwave driving signal at the instant in time when the electron is injected into the guide.

We have modified the gun design by additional elements that allow us to operate it either in a continuous or a pulsed mode with electron pulse durations of several 100 ps (see Sec. V A for further details) and output beam currents on the order of several femtoamperes [34].

The electrodes of the guiding chip are $L = 37$ mm long and bent along a curve with a radius of 40 mm, like in Ref. [24]. The microwave signal is delivered to the guiding electrodes by a coplanar waveguide structure on the backside of the chip, which is interconnected to the signal electrodes by plated through-holes with a diameter of 300 μm. An electrically short configuration is established, where a standing microwave signal forms on the guiding electrodes as the microwave wavelength $\lambda = 200$ mm is much larger than the electrode length L.The impedance mismatch of the guiding electrodes, with a characteristic impedance of 20 Ω, and the 50-Ω feeding coplanar waveguide structure leads to reflections. Hence, -5.16 dB of the injected microwave power is transmitted to the signal electrodes at $\Omega = 2\pi \times 996$ MHz.

Electrons that leave the exit aperture of the electron gun are injected into the guiding potential above one edge of the substrate. Electrons that are successfully guided propagate along the electrodes and are detected on a phosphor screen behind a microchannel-plate (MCP) detector at the other edge of the substrate [see Fig. 2(a)]. Because of the curved electrode design, the guided electron beam becomes deflected by 21 mm on the MCP with respect to the unguided electrons. Figure 2(b) shows the electron signal recorded by a CCD camera, with the color scale corresponding to the electron count rate. Here the electron energy is $E_{\mathrm{kin}} = 3$ eV, and the guide is operated at the microwave parameters given above. A bright and collimated signal of guided electrons is visible at $x = 0$ mm. Additionally, there is a faint signal of lost electrons that spirals around the guided spot. This structure can be related to electrons that are lost from the guiding potential within the curve on their way to the detector. As can be seen from Figs. 1(b) and 1(c), the pseudopotential is weakest along the z direction, which is the normal of the substrate plane. For this reason, electrons are preferentially lost in the vertical z direction and, therefore, are detected at larger z with respect to the guided electrons. The earlier electrons get lost on their curved path, the less they are deflected along the x axis. Accordingly, lost electrons are detected in between the guided and unguided signal of electrons, which is detected at $x = 21$ mm when the microwave drive of the guiding chip is turned off (not shown). Figure 2(c) shows a simulated guiding signal that we obtain from particle-tracing simulations. As can be seen, the simulated guiding signal is in good accordance with the electron signal observed in the experiment. In the next section, we give a detailed description of the underlying particle-tracing simulations and discuss the characteristic motion of electrons in the guiding potential.

III. COMPARISON OF GUIDING SIGNAL TO TRAJECTORY SIMULATIONS

We investigate the dynamics of electrons after injection into the guiding potential by performing particle-tracing simulations and comparing these to the measured guiding signal. By these means, we are able to identify the origin of an excited electron motion, which may result in a loss of electrons from the guiding potential.

Ideally, an electron traveling perfectly on axis with the minimum of the guiding potential should propagate along the guide without experiencing any electric fields and should, therefore, not be subjected to any forces. Figure 3 shows a simulation of the absolute maximum electric-field amplitude $|\mathbf{E}|$ close to the substrate edge. As can be seen, at a y position larger than approximately 3 mm, where the guiding potential is fully developed and not influenced by edge effects anymore, the quadrupolar shape of the electric field results in an electric field null at a height of $R_0 = 500$ μm above the substrate. However, due to the termination of the electrode design close to the substrate edge located at $y = 0.5$ mm, fringing electric fields are present on the guide axis between the electron gun and the microwave chip. As a consequence, an electron impinging at a height of $R_0 = 500$ μm experiences an electric field in the vertical z direction and becomes deflected prior to injection into the guiding potential. This will lead to an unwanted excited motion of the injected electron inside the guiding potential, no matter how good an electron beam the electron source is able to deliver. Hence, the impact of these fringing fields during electron injection has to be minimized.

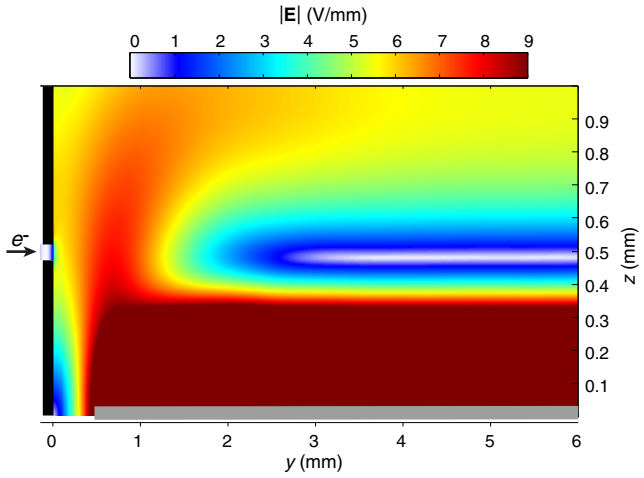

FIG. 3. Simulation of electric fields close to the substrate edge where electrons are injected into the guiding potential. The color scale displays the absolute value of the electric field $|\mathbf{E}|$ at a snapshot in time where it is at its maximum. The last aperture of the electron gun is shown schematically at $y = 0$ mm (drawn in black). The microwave substrate at $z = 0$ mm is indicated in gray starting from $y = 0.5$ mm. Fringing fields near the substrate edge lead to significant local deviations of the electric field from the ideal quadrupolar shape. As a consequence, an electron impinging at a height $R_0 = 500$ μm experiences an electric-field amplitude E and becomes deflected during injection.

The particle trajectories are simulated using the commercially available boundary element method solver CPO. These simulations take into account the electric field oscillating at the microwave driving frequency and are performed according to the experimental parameters described above. Figures 4(a) and 4(b) show a side view of the corresponding electron trajectories in the vertical

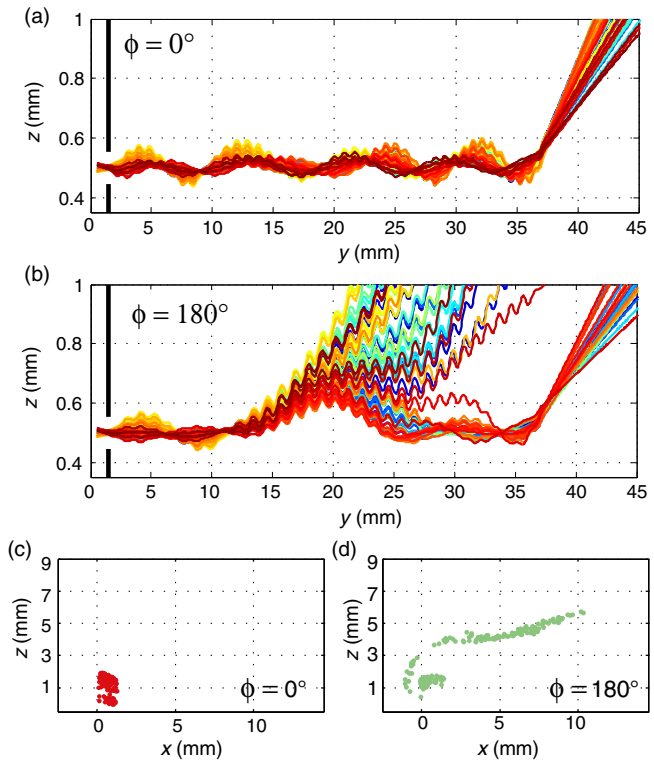

FIG. 4. Electron trajectory simulations resolving the phase of the microwave drive. Electrons enter the guiding potential at $y = 0$ mm through the exit aperture of the electron gun (drawn in black) at a height of $z = 500$ μm above the substrate. The initial electron spot size in the simulations is 60 μm in diameter. After propagation through the guiding potential, electrons are released into free space at $y = 37$ mm and detected in the detector plane at $y = 45$ mm (not shown). (a),(b) show a side view of ray-tracing simulations in the y-z plane along the guiding electrodes. The color of the electron trajectories is chosen for better visibility and does not contain any further information here. (a) For a microwave phase of $\phi = 0°$, all electrons are confined in the guiding potential and oscillate with the trap frequency ω corresponding to a spatial period of approximately 9.5 mm. In (b), a significant portion of electrons is lost for a microwave phase of $\phi = 180°$. Here electrons are lost from the guiding potential in the vertical z direction starting from $y = 15$ mm. (c),(d) show the simulated guiding signals for the corresponding microwave phases. In (c), for $\phi = 0°$, all trajectories are guided along the curve and hit the detector around $x = 0$, whereas in (d), a large fraction of the trajectories is lost for $\phi = 180°$.

y-z plane along the guiding electrodes. Electrons with a kinetic energy of 3 eV are injected into the guide at $y = 0$ mm, where the last aperture of the gun is shown schematically and exit the guide at $y = 37$ mm. As can be seen, the electron trajectories are dominated by the slow secular motion in the guiding potential given by the trap frequency ω and discernable as oscillations with a spatial period of approximately 9.5 mm at this particular electron velocity. On top of that harmonic motion, the fast micromotion of electrons can be identified with much smaller oscillation amplitude and oscillating at the driving frequency Ω. The oscillations of the micromotion have a spatial period of approximately 1 mm.

The unwanted fringing electric fields close to the substrate edge oscillate with the driving frequency Ω of the microwave drive. Furthermore, an electron experiences less than a single cycle of the driving electric field on the first millimeter between the gun exit and the guiding chip where the amplitude of the fringing fields is largest. For this reason, the initial deflection and the resulting oscillation of the electron within the guiding potential depend highly on the orientation and the amplitude of the fringing electric fields and, hence, the phase of the microwave driving signal. This becomes apparent in the particle-tracing simulations when electron trajectories are released at different times with respect to the phase of the microwave driving signal. Depending on this phase, electrons experience a different orientation of the electric-field amplitude during injection, which governs the passage into the guiding potential. The particle-tracing simulations are performed for a set of different release times covering a full evolution of 2π in the microwave phase.

Figure 4(a) shows trajectories for a microwave phase of $\phi = 0^\circ$ where all electrons are tightly confined by the guiding potential. In contrast, in Fig. 4(b), for $\phi = 180^\circ$, a large fraction of electrons is lost, starting from $y =$ 15 mm, on their way to the detector in the vertical z direction. The phase dependence of the electron guiding efficiency observed in these simulations can be attributed to electric fringing fields at the edges of the guiding substrate. For microwave phases around $\phi = 0^\circ$, a relatively small initial deflection results in the characteristic oscillation of electrons in the guiding potential. In contrast, for microwave phases close to $\phi = 180^\circ$, electrons experience a stronger initial deflection, giving rise to a loss of electrons from the guide.

From the same particle-tracing simulations, we can infer the location of electrons impinging on the detector. In Fig. 2(c), a simulated guiding signal is shown. Here the color scale displays the relative phase ϕ of the microwave electric field. The simulations reproduce the general structure of the experimental guiding signal shown in Fig. 2(b) very well. In addition, Fig. 2(c) illustrates that depending on the relative phase of the electric field, electrons can either be guided (signal around $x = 0$ mm) or lost. This is more apparent in Figs. 4(c) and 4(d), where the corresponding detector signals are shown for two distinct microwave phases. For $\phi = 0^\circ$, all electrons are guided and reach the detector around $x = 0$ mm, whereas for $\phi = 180^\circ$, a significant portion of electrons is lost. This portion corresponds to the trajectories that are lost along the z direction in Fig. 4(b).

In the following sections, we present a viable approach to reduce the amplitude of the transversally excited electron motion by minimizing forces that initially deflect the electron beam. First of all, we perform a numerical optimization of the shape of the chip electrodes in order to reduce the amplitude of unwanted fringing fields. Then we experimentally employ a pulsed electron source to temporally synchronize the injection of electron pulses to a certain microwave phase. By these means, we can control the specific orientation of the driving electric field during electron injection and, hence, increase the guiding efficiency.

IV. OPTIMIZED ELECTRODE DESIGN FOR ELECTRON INJECTION

The pseudopotential shown in Fig. 1(a) is simulated assuming infinitely long electrodes along the longitudinal y direction. In the case of finite electrode length, where the electrodes are terminated 0.5 mm before the substrate edge, we observe a significant deterioration of the guiding potential by fringing electric fields (see Fig. 3).

In order to reduce the unwanted fringing fields and to provide a smooth transition for electrons from the exit aperture of the electron gun into the guiding potential, we perform a numerical optimization of the electrode layout. Using a Nelder-Mead simplex algorithm, we minimize a merit function M by systematic variation of the position of a predetermined number of N points, which parametrize the shape of the chip electrodes in the vicinity of the substrate edge (see Fig. 5).

Figure 5(a) shows the electrode design close to the substrate edge that is obtained by an initial optimization [24] and is used for the experiments described in Secs. II, III, and V. This electrode layout is obtained from minimizing the vertical fringing electric fields E_z using $N = 6$ adjustable points. The optimization is performed using a merit function M that is given by the integrated vertical electric-field amplitude E_z on the first 15 mm along the electrodes $M = \int |E_z| dy$. As can be seen from the corresponding pseudopotential simulation in Fig. 5(c), the pseudopotential minimum bends down when approaching the substrate edge from within the guide. Close to the substrate edge, the pseudopotential minimum R_0 is reduced to about 490 μm, whereas 15 mm along the electrodes, it is located at 500 μm, as for the ideal case of infinitely long wires. More importantly, the potential depth is simultaneously reduced when approaching the substrate edge. This even leads to a repelling potential curvature on the first

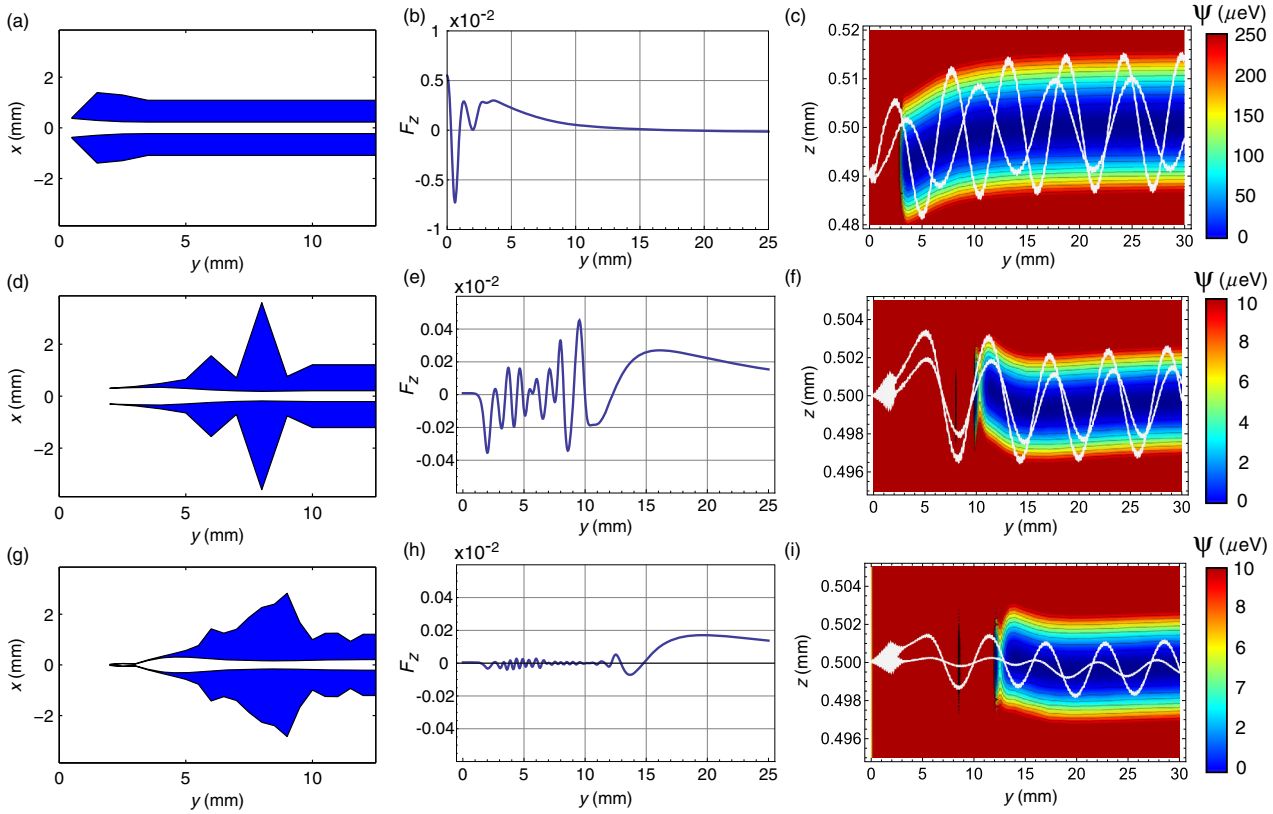

FIG. 5. Conductor layout, vertical pseudopotential gradient along the guide axis, and electron-trajectory simulations for optimized coupling structures. In (a),(d),(g), the signal electrodes are drawn in blue, whereas white corresponds to grounded areas (gapless-plane approximation). In the numerical optimization of the electrode shape, the width of each electrode is constrained to be larger than 20 μm. In (b),(e),(h), the dimensionless, vertical pseudopotential gradient F_z is shown. The last column (c),(f),(i) shows simulated trajectories (white curves) together with a color plot of the pseudopotential. For better visibility, trajectories are shown for two selected microwave phases where the electron performs the most- and the least-excited oscillation within the guiding potential. Note the different scaling of the z axis as well as the color scale going from Figs. 5(c) to 5(f) and 5(i). Clearly, the reduction in the vertical pseudopotential gradient is reflected in a smaller oscillation amplitude of the electron after injection.

1 mm away from the substrate edge (not shown). After 15 mm along the electrodes, however, the guiding potential already matches the ideal potential of infinitely long electrodes to within 1 meV.

For a further optimization, we use the freely available Surface Pattern package [35–37], which is implemented in MATHEMATICA to simulate the electric field of the guiding structure in the gapless-plane approximation [38]. This package is capable of yielding analytic results for any planar electrode structure [39], making optimizations fast. In the subsequent optimizations, the figure of merit is chosen such that its minimization will lead to the reduction of the normalized, dimensionless ponderomotive gradient force in the vertical z direction

$$F_z = \frac{4M\Omega^2 R_0^3}{Q^2 V_0^2}\frac{\partial}{\partial z}\Psi.$$

This ponderomotive force deflects the incoming electron in the vertical z direction where the confinement is weakest. There is no deflection in the x direction due to the symmetry of the electrode layout. The merit function M of the optimization is, therefore, given by the integration of the vertical gradient force on the first 15 mm along the electrodes $M = \int |F_z| dy$.

The gradient force F_z strongly depends on the vertical electric field E_z. However, according to Maxwell's equations, changing the electric field E_z in the vertical z direction along the guide axis is directly reflected in a changing longitudinal field E_y along the y direction (in the x direction, no field is possible due to the planar electrode symmetry). As a result, the optimization algorithm seeks to increase E_y by introducing a longitudinal field gradient along y. A zigzag-shaped electrode layout produces such a longitudinal gradient and may, therefore, effectively reduce F_z. The field gradient in the y direction obtained from the optimized electrode shape leads to a temporary deceleration of the electron beam on the order of several 10 meV.

The left column of Fig. 5 shows the result of the electrode design optimization with increasing number N of points along the electrode edges. From Fig. 5(a) with the initial design using $N = 6$ points to Fig. 5(d) with $N = 15$,

there is a reduction in the maximum normalized gradient force F_z by a factor of 17. The improved properties of the electrode design in Fig. 5(d) can be mainly attributed to the modified merit function, the increased length of the optimized electrode taper from 3 to 8 mm, and the increased distance between the substrate edge and electrodes from 0.5 to 2 mm. The adjustable points in both designs are equally spaced along the guide axis by 1-mm distance. We have checked that further increasing the taper length does not yield a significantly improved merit function.

The electrode design in Fig. 5(g), which features a decreased spacing of 0.5 mm between the optimization points and a total of $N = 39$ points, shows another reduction in the maximum normalized gradient force by a factor of 3 with respect to Fig. 5(d).

The Nelder-Mead simplex algorithm does not necessarily converge towards a global minimum. The optimum electrode shape depicted in Fig. 5(g) may, therefore, correspond only to a local minimum. Future optimizations of the electrode shape employing other optimization algorithms might converge towards a global minimum and, hence, reduce fringing fields even further.

The effect of the electrode optimization becomes clearly visible in particle-trajectory simulations for the different geometries. The last column of Fig. 5 shows simulated trajectories for an electron with a kinetic energy of 1 eV, incident parallel to the guide axis, together with a color plot of the pseudopotential in the y-z plane. The trajectories are calculated taking into account the simulated electric fields and assuming a driving frequency of $\Omega = 2\pi \times 2.8$ GHz and a voltage amplitude of $V_0 = 72$ V. This results in a transverse frequency $\omega = 2\pi \times 100$ MHz, a potential depth $U = 23$ meV, and a stability parameter $q = 0.1$ of the guiding potential. Compared to the experiments presented in this paper, the microwave parameters of the particle-tracing simulations are tuned to yield a smaller stability parameter q at a similar trap frequency ω and potential depth U. Effectively, this leads to a more cycle-averaged motion of the electron due to the increased microwave driving frequency. This results in similar dynamics of the electron within the guiding potential (similar trap frequency). However, the effects that are related to the phase of fringing fields are reduced during the electron injection, as is the micromotion inside the guiding potential. We show particle trajectories for two specific phases in the last column of Fig. 5, for which the effect of the fringing fields is maximized and minimized.

For the initial design (first row of Fig. 5), an electron incident on the guiding structure is exposed to relatively strong vertical fringing fields. This leads to an excitation of the electron within the guiding potential with an oscillation amplitude of $\delta z = 9.5$ μm to $\delta z = 14$ μm, depending on the microwave phase. Going to $N = 15$ points (second row in Fig. 5) yields a reduction of the on-axis gradient force that is directly reflected in a smaller oscillation amplitude of $\delta z = 1.4$ μm to $\delta z = 2.88$ μm. For the best optimization result with $N = 39$ points (last row in Fig. 5), the excitation of the electron oscillation is even further reduced and amounts to an amplitude of $\delta z = 400$ nm to $\delta z = 1.4$ μm. Taking into account the trajectories for many different phases, we find that 25% of the trajectories oscillate with an amplitude smaller than 500 nm for the best optimization result with $N = 39$ points. More specifically, we can deduce from this phase dependence that within a time window of 40 ps, all electrons can be injected with an oscillation amplitude below 500 nm by synchronized injection of electron pulses.

The transverse oscillation amplitude of $\delta z = 400$ nm is comparable to the width $\Delta z = \sqrt{\hbar/(2M\omega)} = 303$ nm of the quantum-mechanical ground state of the harmonically approximated pseudopotential. This indicates that classical particle-tracing simulations hit the limits of applicability and that the transverse motion of the electron has to be described by quantized eigenstates of the guiding potential. Quantum control over the transverse motion of guided electrons is of utmost interest, as these motional quantum states can be used as a carrier of quantum information in future experiments like guided matter-wave interferometry or controlled interactions with a specimen in close vicinity of the guiding chip.

The particle-tracing simulations suggest that, by temporally synchronizing the injection of electron pulses to a specific phase of the driving electric field, the excited motion of an electron inside the guide can be minimized to a regime that allows the direct injection into low-lying quantum states of the transverse guiding potential. As a first but essential step towards this goal, we experimentally demonstrate the synchronization of a pulsed electron source to the phase of the driving field of the microwave guide and present phase-resolved measurements of the electron guiding efficiency in the next section.

V. MICROWAVE PHASE-RESOLVED ELECTRON INJECTION

A. Pulsed electron gun

We have built a pulsed electron source that can be synchronized to the microwave driving signal of the electron guide. As a result, all electrons that are injected into the guiding potential experience the same orientation of the oscillating electric field. This holds true if the electron pulse duration is small compared to a single cycle at the microwave driving frequency with a period of approximately 1 ns.

In order to resolve a single cycle of the microwave field, we implement a fast deflection element into the conventional electron-gun design, similar to a streak camera [see Fig. 6(a)]. We use three rectangular apertures to deflect the beam along the z direction. The center electrode is isolated such that we can apply a deflection voltage $+V_{\mathrm{defl}}$ to the

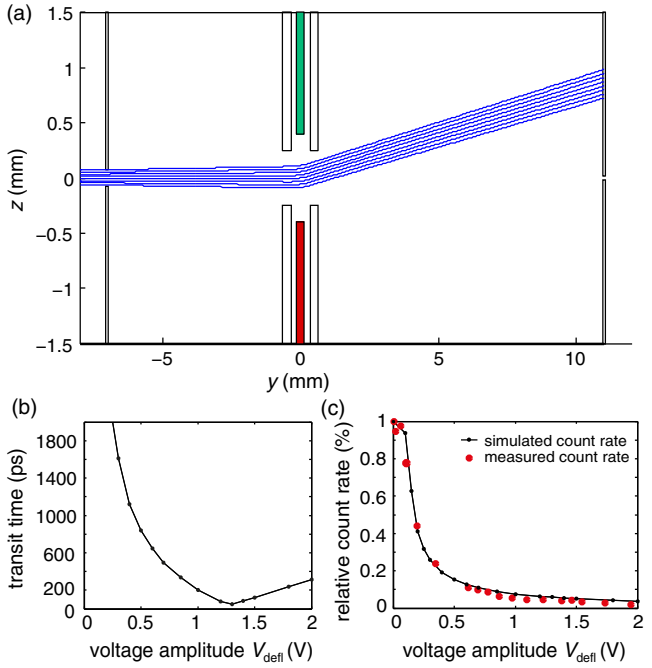

FIG. 6. Pulsed electron source. (a) Schematic of the deflection element together with results of a particle-tracing simulation (blue trajectories). The trajectories are simulated with a static deflection voltage of 0.5 V applied to the upper (green) and −0.5 V to the lower (red) deflection electrode. The electron beam enters through an aperture at $y = -7$ mm with a diameter of 150 μm and becomes deflected onto the exit aperture with a diameter of 50 μm at $y = 11$ mm. Only electrons that pass through the exit aperture, which is just visible at $z = 0$ mm, are later injected into the guide. (b) Simulated transit time as a function of the deflection voltage V_{defl}. A minimum transit time of 51 ps can be reached by applying $V_{\mathrm{defl}} = 1.3$ V. (c) Simulated (black) and measured (red) electron count rate after the exit pinhole as a function of V_{defl}.

upper part (drawn in green) and $-V_{\mathrm{defl}}$ to the lower part (drawn in red) of the electrode. The other two rectangular apertures are grounded. Note that these electrodes are not rotationally symmetric but have a planar symmetry along the x axis. Figure 6(a) shows a particle-tracing simulation where a static deflection voltage of $V_{\mathrm{defl}} = 0.5$ V is applied to the deflection element. Obviously, in this setting no electrons will pass the last aperture with a diameter of 50 μm. When an alternating microwave field with amplitude V_{defl} and angular frequency Ω_{defl} is applied to the deflection element, the electron beam is repeatedly swept over the exit aperture. Therefore, electron bunches are generated every time the beam passes over the exit pinhole. With increasing deflection amplitude, the velocity at which the electron beam passes over the exit aperture rises, leading to shorter electron bunches behind the exit of the gun. At the same time, we expect a decrease in the electron count rate.

The electron pulse duration of the gun is given by the time interval that the electron beam spends over the exit aperture during one cycle of the deflection element. In the following, we simulate particle trajectories in order to extract the maximum time-of-flight difference between two electrons that leave the gun during one cycle. However, these simulations are performed for a monochromatic electron beam with a kinetic energy of 3 eV. The pulse duration obtained by these means does not account for the longitudinal energy spread of the electron source and depends only on the geometry of the deflection element, the electron energy, and the deflection amplitude V_{defl}. We, therefore, refer to the pulse duration obtained by monochromatic particle-tracing simulations as the transit time interval. In order to determine the actual electron pulse duration, we also have to consider the longitudinal energy spread of the electron source and take into account dispersion within the deflection element. We call this time interval, which includes chromatic effects, the electron pulse duration. After presenting the particle-tracing simulations and an experimental characterization of the deflection element, we discuss the longitudinal energy spread of the source, which turns out to currently limit the electron pulse duration of the gun.

We perform particle-tracing simulations for a deflection frequency of $\Omega_{\mathrm{defl}} = 2\pi \times 99.6$ MHz and varying deflection amplitudes V_{defl}. We choose $\Omega_{\mathrm{defl}} = 2\pi \times 99.6$ MHz, i.e., one-tenth of the guide's drive frequency, in order to make sure that an electron experiences only one single cycle of the deflection amplitude while passing through the deflection element. From these simulations, we can extract the duration that the monoenergetic electron beam spends over the exit aperture and determine the transit time interval. As depicted in Fig. 6(b), these simulations show a decrease in the transit time for increasing deflection amplitudes until a minimum is reached at $V_{\mathrm{defl}} = 1.3$ V, corresponding to a time interval of 51 ps. The linear increase of the transit time for $V_{\mathrm{defl}} > 1.3$ V is due to electric fields along the optical axis that are created by the deflection element. These fields lead to an acceleration of electrons passing close by the positive deflection electrode, whereas electrons close to the negative electrode are decelerated. As one would expect, this effect increases the transit time linearly with the electric-field amplitude.

The deflection element is manufactured from a printed circuit-board substrate. Signals can be applied to the deflection electrodes by microwave-compatible coplanar waveguide structures. Therefore, we can sweep the electron beam at microwave frequencies over the exit aperture. Since we cannot directly measure the transit time interval, we can only compare the measured and simulated drop in electron count rate as a function of the deflection amplitude after the last aperture. This is an indirect measurement of the transit time interval. As can be seen from Fig. 6(c), the measured drop in electron count rate agrees very well with the ray-tracing simulation results. In the following experiments, we set $V_{\mathrm{defl}} = 1.46$ V, corresponding to a

transit time of 105 ps, since this yields experimentally the best compromise between pulse duration and electron count rate.

So far, the particle-tracing simulations are based on a perfectly monochromatic source. The electron gun, however, is based on a conventional tungsten-filament thermionic emitter. The longitudinal full width at half maximum (FWHM) energy spread of such a source is $\Delta E = 2.446\ k_B T = 0.53$ eV at a temperature $T = 2500$ K [40]. This results in a time-of-flight distribution with FWHM of $\Delta t = d\sqrt{M/2}[1/(E-\Delta E/2) - 1/(E+\Delta E/2)] = 693$ ps. Here, d is the distance between the deflection element and the exit aperture. Consequently, the electron pulse duration is limited by the dispersive nature of the electron source rather than the deflection element itself.

B. Phase-resolved guiding signal

This section demonstrates a phase-resolved measurement of the electron guiding efficiency using the electrode design shown in Fig. 5(a). In order to inject electrons at one specific phase of the microwave driving signal, synchronicity between the pulsed source and the microwave drive of the guide has to be maintained. In the following experiment, this can be realized if the phase of the microwave drive Ωt and the phase of the deflection element $\Omega_{\mathrm{defl}} t$ obey the condition $\Omega t + \Delta\phi = 2n\Omega_{\mathrm{defl}} t$, where $\Delta\phi$ is a constant phase shift, and n is an integer number.

Figure 7 shows a schematic of the experimental setup. We phase lock two analog signal generators and separately drive the microwave guide at a frequency Ω and the pulsed source at Ω_{defl}. In order to achieve synchronous electron injection (as described above), we set $\Omega = 2\pi \times 996$ MHz and $\Omega_{\mathrm{defl}} = 2\pi \times 99.6$ MHz, corresponding to $n = 5$. By inserting a variable phase shifter in the microwave drive of the guide, we can shift the microwave phase of the guide relative to that of the pulsed source by a constant phase $\Delta\phi$.

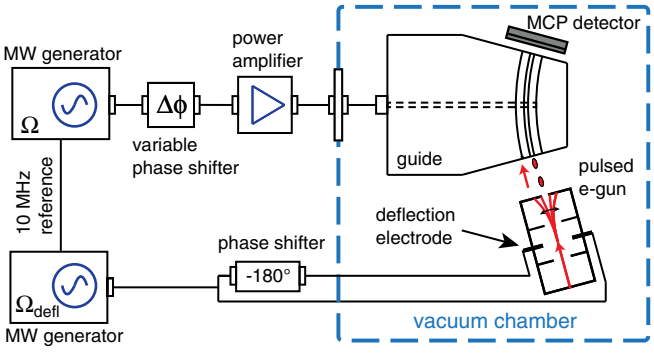

FIG. 7. Schematic of the microwave phase-resolved measurement setup. A stable phase lock is established via the 10-MHz reference signal between two analog signal generators in order to separately drive the microwave guiding chip and the pulsed source. We insert a variable phase shifter in the signal path of the guiding chip to shift the microwave phase of the guide relative to the pulsed source. The $-180°$ phase shifter in the signal path of the pulsed electron source yields an opposite sign of the deflection voltage V_{defl} on the upper and lower part of the deflection element.

Figure 8(a) shows two measured guiding signatures for $\Delta\phi = 3°$ and $\Delta\phi = 185°$. It can clearly be seen that the number of guided electrons as well as the number of lost electrons are strongly influenced by the phase $\Delta\phi$.

In Fig. 8(b), a quantitative measurement of the phase-dependent electron injection is shown. The red triangles (blue dots) correspond to the relative change of the integrated count rate of guided (lost) electrons as a function of the relative phase $\Delta\phi$. This measurement shows that the injection of electrons is highly dependent on the microwave phase and, hence, the orientation of the electric-field amplitude during injection. The two curves corresponding to the integrated guided and lost electron signals are shifted in phase by 180° to each other. This confirms that we can increase (decrease) the electron guiding efficiency by controlling the relative phase $\Delta\phi$. Note that these observations cannot be explained by a spurious loss mechanism that just occurs for certain settings. The red (blue) lines correspond to sinusoidal fits from which we infer the contrast of the modulated guided (lost) electron signal to be

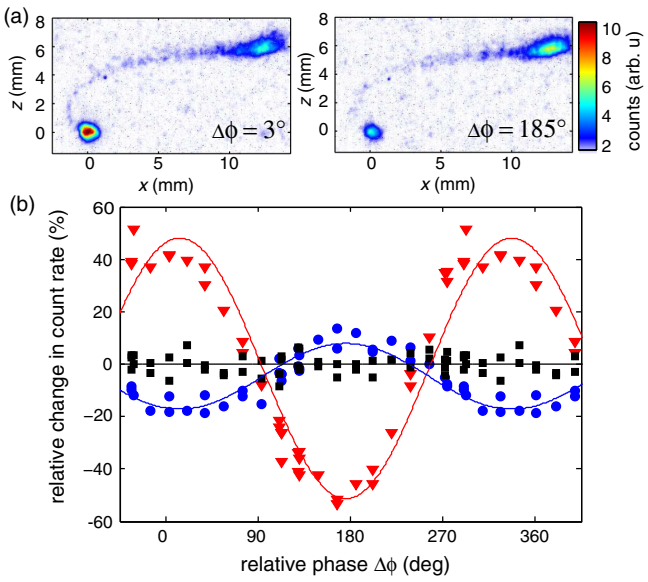

FIG. 8. Microwave phase-resolved measurements. (a) Electron signals are shown for $\Delta\phi = 3°$ and $\Delta\phi = 185°$ where the number of guided electrons is at its maximum and minimum with respect to the microwave phase $\Delta\phi$. (b) Relative change in count rate of guided (red triangles) and lost (blue dots) electrons as a function of the relative microwave phase for synchronous operation of the electron gun. When the gun is operated in asynchronous mode, with $\Omega_{\mathrm{defl}} = \Omega/(2n) + 2\pi \times 1$ mHz, we observe no change in the guided and unguided signal (black squares). Every data point is an average over 240 images with 1-s exposure time which corresponds to 4.78×10^{10} electron pulses. The lines correspond to sinusoidal fits of the measured data.

50% (13%). The discrepancy in the contrast of the guided and unguided signal can be attributed to the fact that not all electrons that are lost from the guide are detected by the MCP detector.

In order to verify that the above measurement relies on a phase-resolved, synchronous measurement, we carry out the exact same measurement with asynchronous phases. The result is shown as black squares in Fig. 8(b). No modulation is observed.

The phase-resolved measurement described above demonstrates a viable strategy to minimize the impact of unwanted fringing electric fields on the transverse electron motion after injection into the guide. The synchronized timing of electron pulses to a certain microwave phase in combination with a numerically optimized electrode design should allow us to inject electrons directly into the transverse quantum ground state of the guiding potential. Additionally, the direct injection into the motional ground state will require diffraction-limited electron optics in order to match the wave function of an impinging electron wave packet to the ground state of the guiding potential. In the outlook, we will discuss prospects of the combination of a pulsed electron source with diffraction-limited electron optics.

VI. CONCLUSION AND OUTLOOK

We show that the transverse motion of electrons after injection into the microwave guide is governed by fringing electric fields that are present close to the substrate edge. During the passage from the electron gun into the guiding potential, an electron is exerted to the fringing fields and becomes deflected prior to injection into the guide. From particle-tracing simulations, we verify that the excited motion of guided electrons depends on the phase of the fringing fields. By synchronizing the injection of electron pulses to a specific phase of the microwave drive, the transverse oscillation amplitude of guided electrons is minimized. However, depending on the precise shape of the guiding electrodes, the electrons still experience vertical electric fields. For this reason, we numerically optimize the chip electrodes close to the substrate edge in order to minimize the amplitude of the unwanted fringing fields. Simulating particle trajectories for the optimized electrode design, we find that the effect of the fringing fields can be minimized to a regime where the transverse oscillation amplitude of the electron is comparable to the spatial extension of the motional quantum ground state of the guiding potential. Hence, a quantum-mechanical description of the transverse electron motion is now required, which will be the scope of future work. As a consequence, the direct injection of electrons into the transverse motional ground state of the guiding potential should be feasible, ultimately allowing for a new class of electron-based quantum-optics experiments

We conclude by giving an outlook on the important prerequisites for an entirely new matter-wave quantum system based on the precise control of slow electrons in the energy range below 10 eV. The techniques described in this paper demonstrate the possibility to provide an adiabatic injection of electrons into the guide. To realize direct ground-state injection using the optimized guiding electrodes, new microwave substrates must be developed that allow us to drive the guide with $\Omega = 2\pi \times 2.8$ GHz and $V_0 = 72$ V. Currently, electron guiding experiments are restricted to electrically short structures, which limits the drive frequencies to $\Omega < 2\pi \times 1.25$ GHz. To this end, impedance-matched, electrically long guiding structures are required where traveling microwave signals are taken into account [25].

Moreover, the direct injection into the motional quantum ground state of the guiding potential imposes stringent requirements on the electron-optical properties of the electron gun. In order to achieve direct injection into the quantum ground state, slow electron wave packets have to perfectly overlap the momentum and spatial wave function of the harmonic guiding potential. For a trap frequency of $\omega = 2\pi \times 100$ MHz, an electron wave packet has to be focused to a spot $\Delta x = \sqrt{\hbar/(2M\omega)} = 303$ nm and collimated to an angle $\alpha = \Delta p/p = \sqrt{\hbar\omega/E_{\mathrm{kin}}} = 0.32$ mrad, where Δp is the momentum spread of the ground state, and p the longitudinal electron momentum at a kinetic energy of 1 eV. The product of Δx and Δp obey the minimum possible measurement uncertainty imposed by the Heisenberg uncertainty relation, which represents the diffraction limit for matter waves.

A semiclassical picture provides the physical properties required for direct ground-state injection more intuitively. A 1-eV electron travels with a longitudinal velocity $v_y = 593$ km/s. Direct injection into the quantum ground state requires the transverse velocity component be smaller than $v_x = 191$ m/s, given by the expectation value of the transverse kinetic energy $\langle E_{\mathrm{kin}} \rangle = \hbar\omega/4 \sim 0.1\,\mu$eV. The velocity ratio v_x/v_y yields the required collimation angle α.

In order to combine the timing of 40-ps electron pulses with diffraction-limited electron optics, we are currently setting up a new, home-built electron source that is based on a metal-nanotip electron emitter. Nanometric tungsten tips are shown to be coherent point sources of electrons, providing exceptionally bright electron beams in dc field emission [41,42]. The appropriate electron optics comprising a focusing Einzel lens together with a quadrupole deflector and a deceleration stage is currently tested. The corresponding particle-tracing simulations at kinetic energies down to 1 eV suggest that, due to sufficiently low aberrations, focusing close to the diffraction limit should be possible. As an important feature, the lens design allows optical access to the nanotip. Hence, the temporal timing of electron pulses can be achieved by laser-triggered electron emission, which should allow the

generation of electron pulses in the sub-100-fs range [43–45].

One potential application of such a guided matter-wave system could be the nondestructive imaging of biological samples with a quantum electron microscope, as recently proposed [26,46]. Here, quantum effects in the motion of electrons that are confined by a microstructured, transverse guiding potential can be exploited to consecutively probe a sample without damage.

ACKNOWLEDGMENTS

We thank R. Schmied for discussions and making the Surface Pattern package available to us. The authors would also like to thank M. Krüger for his critical reading of the manuscript. This research is funded in part by the Gordon and Betty Moore Foundation.

[1] C. Davisson and L. H. Germer, Diffraction of electrons by a crystal of nickel, Phys. Rev. **30**, 705 (1927).
[2] L. Marton, J. A. Simpson, and J. A. Suddeth, Electron beam interferometer, Phys. Rev. **90**, 490 (1953).
[3] G. Möllenstedt and H. Düker, Fresnelscher Interferenzversuch mit einem Biprisma für Elektronenwellen, Naturwissenschaften **42**, 41 (1955).
[4] H. Kiesel, A. Renz, and F. Hasselbach, Observation of Hanbury Brown–Twiss anticorrelations for free electrons, Nature (London) **418**, 392 (2002).
[5] P. Sonnentag and F. Hasselbach, Measurement of decoherence of electron waves and visualization of the quantum-classical transition, Phys. Rev. Lett. **98**, 200402 (2007).
[6] J. Chiaverini, R. B. Blakestad, J. Britton, J. D. Jost, C. Langer, D. Leibfried, R. Ozeri, and D. J. Wineland, Surface-electrode architecture for ion-trap quantum information processing, Quantum Inf. Comput. **5**, 419 (2005).
[7] D. Leibfried, R. Blatt, C. Monroe, and D. Wineland, Quantum dynamics of single trapped ions, Rev. Mod. Phys. **75**, 281 (2003).
[8] D. J. Wineland and D. Leibfried, Quantum information processing and metrology with trapped ions, Laser Phys. Lett. **8**, 175 (2011).
[9] H. Häffner, C. F. Roos, and R. Blatt, Quantum computing with trapped ions, Phys. Rep. **469**, 155 (2008).
[10] J. Reichel and V. Vuletic, *Atom Chips* (Wiley-VCH, Berlin, 2011).
[11] W. Hänsel, J. Reichel, P. Hommelhoff, and T. W. Hänsch, Trapped-atom interferometer in a magnetic microtrap, Phys. Rev. A **64**, 063607 (2001).
[12] M. D. Hughes, B. Lekitsch, J. A. Broersma, and W. K. Hensinger, Microfabricated ion traps, Contemp. Phys. **52**, 505 (2011).
[13] J. Amini, J. Britton, D. Leibfried, and D. J. Wineland, in *Atom Chips*, edited by J. Reichel and V. Vuletic (Wiley-VCH, Berlin, 2011).
[14] K. R. Brown, C. Ospelkaus, Y. Colombe, A. C. Wilson, D. Leibfried, and D. J. Wineland, Coupled quantized mechanical oscillators, Nature (London) **471**, 196 (2011).
[15] M. Harlander, R. Lechner, M. Brownnutt, R. Blatt, and W. Hänsel, Trapped-ion antennae for the transmission of quantum information, Nature (London) **471**, 200 (2011).
[16] A. P. VanDevender, Y. Colombe, J. Amini, D. Leibfried, and D. J. Wineland, Efficient fiber optic detection of trapped ion fluorescence, Phys. Rev. Lett. **105**, 023001 (2010).
[17] T. H. Kim, P. F. Herskind, and I. L. Chuang, Surface-electrode ion trap with integrated light source, Appl. Phys. Lett. **98**, 214103 (2011).
[18] P. F. Herskind, S. X. Wang, M. Shi, Y. Ge, M. Cetina, and I. L. Chuang, Microfabricated surface ion trap on a high-finesse optical mirror, Opt. Lett. **36**, 3045 (2011).
[19] J. True Merrill, C. Volin, D. Landgren, J. M. Amini, K. Wright, S. C. Doret, C. -S. Pai, H. Hayden, T. Killian, D. Faircloth, K. R. Brown, A. W. Harter, and R. E. Slusher, Demonstration of integrated microscale optics in surface-electrode ion traps, New J. Phys. **13**, 103005 (2011).
[20] C. Ospelkaus, U. Warring, Y. Colombe, K. R. Brown, J. M. Amini, D. Leibfried, and D. J. Wineland, Microwave quantum logic gates for trapped ions, Nature (London) **476**, 181 (2011).
[21] D. T. C. Allcock, T. P. Harty, C. J. Ballance, B. C. Keitch, N. M. Linke, D. N. Stacey, and D. M. Lucas, A microfabricated ion trap with integrated microwave circuitry, Appl. Phys. Lett. **102**, 044103 (2013).
[22] S. X. Wang, J. Labaziewicz, Y. Ge, R. Shewmon, and I. L. Chuang, Demonstration of a quantum logic gate in a cryogenic surface-electrode ion trap, Phys. Rev. A **81**, 062332 (2010).
[23] S. X. Wang, Y. Ge, J. Labaziewicz, E. Dauler, K. Berggren, and I. L. Chuang, Superconducting microfabricated ion traps, Appl. Phys. Lett. **97**, 244102 (2010).
[24] J. Hoffrogge, R. Fröhlich, M. A. Kasevich, and P. Hommelhoff, Microwave guiding of electrons on a chip, Phys. Rev. Lett. **106**, 193001 (2011).
[25] J. Hoffrogge and P. Hommelhoff, Planar microwave structures for electron guiding, New J. Phys. **13**, 095012 (2011).
[26] W. P. Putnam and M. F. Yanik, Noninvasive electron microscopy with interaction-free quantum measurements, Phys. Rev. A **80**, 040902(R) (2009).
[27] T. Laycock, B. Olmos, T. W. A. Montgomery, W. Li, T. M. Fromhold, and I. Lesanovsky, Control of atomic Rydberg states using guided electrons, J. Phys. B **46**, 245502 (2013).
[28] N. Daniilidis, D. J. Gorman, L. Tian, and H. Häffner, Quantum information processing with trapped electrons and superconducting electronics, New J. Phys. **15**, 073017 (2013).
[29] S. Seidelin, J. Chiaverini, R. Reichle, J. J. Bollinger, D. Leibfried, J. Britton, J. H. Wesenberg, R. B. Blakestad, R. J. Epstein, D. B. Hume, W. M. Itano, J. D. Jost, C. Langer, R. Ozeri, N. Shiga, and D. J. Wineland, Microfabricated surface-electrode ion trap for scalable quantum information processing, Phys. Rev. Lett. **96**, 253003 (2006).
[30] F. Hasselbach, Progress in electron- and ion-interferometry, Rep. Prog. Phys. **73**, 016101 (2010).
[31] F. G. Major, V. N. Gheorghe, and G. Werth, *Charged Particle Traps* (Springer, Berlin, 2005).

[32] J. H. Wesenberg, Electrostatics of surface-electrode ion traps, Phys. Rev. A **78**, 063410 (2008).
[33] P. W. Erdman and E. C. Zipf, Low-voltage, high-current electron gun, Rev. Sci. Instrum. **53**, 225 (1982).
[34] As a result of the low electron current, the guiding experiments are performed with one electron at a time so that the electron-electron interaction effects are irrelevant.
[35] See http://atom.physik.unibas.ch/people/romanschmied/code/SurfacePattern.php.
[36] R. Schmied, Electrostatics of gapped and finite surface electrodes, New J. Phys. **12**, 023038 (2010).
[37] R. Schmied, J. H. Wesenberg, and D. Leibfried, Optimal surface-electrode trap lattices for quantum simulation with trapped ions, Phys. Rev. Lett. **102**, 233002 (2009).
[38] We have checked the validity of the gapless-plane approximation by direct comparison to the commercially available boundary element method solver CPO.
[39] Because of the constraints of the field simulation to the planar electrode designs, the electron-gun exit aperture is modeled as a closed conducting electrode located at $y = 0$ mm.
[40] P. W. Hawkes and E. Kasper, *Applied Geometrical Optics*, Principles of Electron Optics Vol. 2 (Academic Press, London, 1989).
[41] M. Fransen, E. Damen, C. Schiller, T. van Rooy, H. Groen, and P. Kruit, Characterization of ultrasharp field emitters by projection microscopy, Appl. Surf. Sci. **94–95**, 107 (1996).
[42] B. Cho, T. Ichimura, R. Shimizu, and C. Oshima, Quantitative evaluation of spatial coherence of the electron beam from low temperature field emitters, Phys. Rev. Lett. **92**, 246103 (2004).
[43] P. Hommelhoff, C. Kealhofer, A. Aghajani-Talesh, Y. R. Sortais, S. M. Foreman, and M. A. Kasevich, Extreme localization of electrons in space and time, Ultramicroscopy **109**, 423 (2009).
[44] A. Paarmann, M. Gulde, M. Müller, S. Schäfer, S. Schweda, M. Maiti, C. Xu, T. Hohage, F. Schenk, C. Ropers, and R. Ernstorfer, Coherent femtosecond low-energy single-electron pulses for time-resolved diffraction and imaging: A numerical study, J. Appl. Phys. **112**, 113109 (2012).
[45] J. Hoffrogge, J. P. Stein, M. Krüger, M. Förster, J. Hammer, D. Ehberger, P. Baum, and P. Hommelhoff, Tip-based source of femtosecond electron pulses at 30 keV, J. Appl. Phys. **115**, 094506 (2014).
[46] S. Thomas, C. Kohstall, P. Kruit, and P. Hommelhoff, Semitransparency in interaction-free measurements, arXiv: 1409.0044.